Marine Structures 70 (2020) 102703

Contents lists available at ScienceDirect

Marine Structures

journal homepage: http://www.elsevier.com/locate/marstruc

Cyclic behavior and strain energy-based fatigue damage analysis of mooring chains high strength steel

Ershad P. Zarandi *, Bjørn H. Skallerud

Department of Structural Engineering, Norwegian University of Science and Technology (NTNU), Richard Birkelands Vei 1A, 7491, Trondheim, Norway

ARTICLE INFO

Keywords:
Strain energy density
Fatigue life prediction
Cyclic plasticity
Hardening/softening
Finite element
Offshore mooring chain

ABSTRACT

This study investigates the low-cycle fatigue behavior of mooring chains high-strength steel grade R4 under different strain amplitudes and strain ratios at room temperature. A fatigue test program has been carried out on small low cycle fatigue specimens cut from large mooring chains. The experimental results characterize the cyclic stress-strain relationship, the mean stress relaxation behavior, and the cyclic plasticity parameters of the material. Strain energy density is correlated with fatigue life through a simple power-law expression and very well represented by Basquin-Coffin-Mansion relationship. Further, a non-linear elastic-plastic material model is calibrated to the experimental stress-strain curves and used for the estimation of energy dissipation in the specimens under applied cyclic loads. The predicted fatigue life using the calibrated material parameters demonstrates a close agreement with the experimental fatigue life. Numerical simulations are carried out to analyze local plastic straining and assess crack initiation at the pit site of corroded mooring chains considering the multiaxial stress state. An energy-based approach is employed to estimate the number of cycles needed for a crack to initiate from an existing corrosion pit.

1. Introduction

In the last decades, energy sources at sea and under the seabed have captured engineering society's attention. As a result, the number of floating offshore production systems and facilities has increased [1]. Continuous operation of these offshore facilities, however, is directly dependent on the integrity of their mooring systems that keep these facilities in position during an operation when subjected to cyclic loads from wave, wind, and current as well as a continuous exposure to a corrosive environment. A mooring line is as strong as its weakest element, and a single line failure increases the load level on the adjacent lines and may cause failure in them ending up with operation shutdown, material loss and risking human life and environment. The high rate of failure of mooring chains used in the offshore industry necessitates improved understanding of phenomena correlated to the fatigue life of these chains, e.g. residual stresses and corrosion, to improve their design and enhance their reliability against failure [1–3]. Nucleation of fatigue cracks generally results from dynamic plastic straining. The amount of plastic straining at the corrosion pit site in mooring chains depends on the applied load as well as the material response to it. The elastic-plastic material behavior under cyclic loading conditions is more complex than that under monotonic loading. Hence, investigation of cyclic response and fatigue properties of mooring chain materials is of great importance to the prediction of the fatigue crack growth rate and the remaining fatigue life of pitted mooring chains.

* Corresponding author.
E-mail address: ershad.p.zarandi@ntnu.no (E.P. Zarandi).

https://doi.org/10.1016/j.marstruc.2019.102703
Received 9 July 2019; Received in revised form 27 November 2019; Accepted 18 December 2019
Available online 7 January 2020

Offshore industry standards (e.g. see Refs. [4,5]) require mooring chains to be proof load (PL) tested to assure their strength capability before being installed offshore. The PL testing involves axially loading the chain up to 70% of its minimum breaking load (MBL), introducing high multiaxial residual stresses (RS) in the chain links. Finite element analysis of the heat treatment process conducted before the PL test has shown that there are RS in all three axial, hoop, and radial directions due to nonhomogeneous plastic deformation caused by different heating/cooling times of the material at the surface and in the core of chain rods [6]. However, the axial RS, which are the largest in magnitude and of high importance as they are normal to the crack faces commonly seen in chain links, are later replaced by greater RS from proof loading. The RS are an influential factor in the remaining life estimation of mooring chains at service and the finite element (FE) simulation of the PL test has revealed that the predicted RS is highly dependent on the chain material, dimensions, and PL level [7–9]. To date, the offshore industry standards lack an explicit consideration of the effects of PL level and material grade on fatigue life of different size mooring chains. An improved model combined with little knowledge of actual residual stresses is sub-optimal and does not bring the fatigue assessment methodology much further. Hence, providing quantitative information on residual stresses and their changes/relaxation in safety-critical components is of high value. This requires a proper material model that accounts for elastic-plastic material response under both monotonic and cyclic loading conditions.

Several investigations have indicated the significance of corrosion on mooring chains fatigue life [10,11]. Some work has been carried out to assess the residual breaking strength of these severely corroded chains, see e.g. Refs. [12,13], and consider the effect of uniform corrosion, as defined in the industry guidelines, on the chains MBL [14]. However, the fatigue strength of the pitted chains is still debatable and not studied. Small corrosion pits can act as stress raisers at the chain link surface, and as a result, reduce the chain fatigue life [15,16]. Numerical investigations on the stress concentration factor of corrosion pits on round bars and flat plates have identified the pit aspect ratio as the main influencing parameter [15–18]. This investigation has been taken further employing experimental observation as well as elastic-plastic material models to determine strain localization and elastic-plastic stress distribution around critical pits and their transition into cracks [19–21]. Nevertheless, strain evolution at the pit site in curved round bars, e.g. mooring chain links, has not been studied to date. Cyclic plasticity and basic fatigue properties for the R4 chain material investigated in the current study are also lacking.

Large-scale fatigue tests have been conducted on both new and used mooring chains in simulated seawater in the past years and the results are presented elsewhere [4,22,23]. However, little attention has been paid to the characterization of the cyclic response of these chain materials. To enhance the understanding of the damage phenomena and mechanisms affecting the fatigue life of offshore mooring chains, e.g. RS and local corrosion, an appropriate material law is essential for accurate prediction of RS and its gradient that has been shown to be influential on fatigue crack growth [8,9,24]. This requires the development of analytical and numerical models along with experimental work. Plastic strain accumulation around pitting holes in mooring chains generally ends in fatigue crack initiation at those locations. Thus, using cyclic material data in FE models, a better prediction of stress gradient around a pit/crack after N cycles of service load is achieved compared to the case where only the monotonic material properties are employed. Moreover, cyclic plasticity tests provide input to the numerical models to quantify RS relaxation over the chains service life.

In this paper, the fatigue properties and cyclic plasticity behavior of mooring chain steel grade R4 is investigated. The tests include strain-controlled fatigue testing at different strain amplitudes and strain ratios of small specimens cut from the straight part of a studless chain link. Section 2 outlines the experimental details and relevant theoretical background. Section 3 provides a comprehensive study of the behavior of the material under various cyclic loads. In addition, plastic/total strain-life curves, as well as cumulative plastic strain energy density (SED)-life curves are constructed based on the fully reversed fatigue test data to estimate the fatigue life of notched and unnotched components. Lastly, in Section 4, finite element simulations are carried out and plastic dissipation at the pit sites on a corroded mooring chain link is investigated. Accordingly, the number of cycles needed for a crack to initiate from an existing corrosion pit is predicted.

2. Methodology

2.1. Experimentation details

Mooring chains high strength steel grade R4 is investigated in this paper. The monotonic mechanical properties of the material are listed in Table 1. The chemical composition of the material can be found in Ref. [25]. Uniaxial strain-controlled cyclic tests were carried out on the samples machined out from the straight part (non-welded side) of an installation chain link with the diameter of 114 *mm* and retrieved from service. The specimens were polished in a drilling machine using first a 320- and then a 600-grit sandpaper.

Table 1
Mechanical material properties of the mooring chain steel grade R4.

Average Vickers hardness (HV10 at 22°*C*)	[HV]	303
Average toughness (Charpy-V at − 20°*C*)	[J]	151
Elasticity modulus ($\boldsymbol{E}$)	[GPa]	207
True yield stress ($\boldsymbol{R_{p0.2}}$)	[MPa]	843
True ultimate stress ($\boldsymbol{R_m}$)	[MPa]	1010
Total extension at maximum force ($\boldsymbol{A_{gt}}$)		0.071
Area reduction		0.68
Poisson's ratio (taken from Ref. [27])		0.3

Table 2
Uniaxial fatigue life of the test specimens at various strain ranges and strain ratios.

ID	Strain range ($\Delta\varepsilon$)	Strain ratio (R_ε)	Cycles to failure (N_f)
Part 1			
T1S6	0.008	−1	15041
T2S5	0.008	−1	9640
T3S3	0.009	−1	4489
T22S24	0.009	−1	7119
T4S2	0.012	−1	3022
T5S15	0.015	−1	1570
T23S7	0.015	−1	1058
T17S19	0.020	−1	646
Part 2			
T21S4	0.008–0.015	−1	10401
Part 3			
T13S22	0.009	0.33	5768
T12S23	0.009	0	6438
T7S13	0.009	−0.33	4877

Table 3
Identified parameters for Ramberg-Osgood relation for mooring chain steel grade R4.

Strain hardening exponent (n)		0.0463
Strain hardening coefficient (K)	[MPa]	1124
Cyclic strain hardening exponent (n')		0.0688
Cyclic strain hardening coefficient (K')	[MPa]	966
Cyclic elasticity modulus (E')	[GPa]	193
Cyclic true yield stress ($R'_{p0.2}$)	[MPa]	630

Table 4
Coffin-Manson fatigue parameters, used in Eq. (3), identified for the mooring chain steel grade R4.

Fatigue strength exponent (b)		−0.0449
Fatigue strength coefficient (σ'_f)	[MPa]	946
Fatigue ductility exponent (c)		−0.6508
Fatigue ductility coefficient (ϵ'_f)		0.725

Table 5
Parameters for non-linear combined kinematic with isotropic hardening model identified for the mooring chain steel grade R4.

	σ_0 [MPa]	Q_∞ [MPa]	b	c [MPa]	γ
Inputs to the optimization routine					
Initial value	500	−200	2	400000	600
Lower band	300	−230	0.5	100000	300
Upper band	700	−170	10	1000000	1600
Calibrated values					
Strain range					
0.008	645	−171	7.6	398702	1234
0.009	546	−227	3.1	536565	1500
0.012	446	−185	1.4	362145	872
0.015	306	−170	5.5	449291	800
0.020	494	−196	4.3	179161	406

The final polishing stage was done longitudinally using a 1000-grit sandpaper to remove circumferential machining marks and generate a smooth surface (with roughness no higher than 0.2 μm). The geometry of the specimens is according to ASTM E606 [26] and illustrated in Fig. 1. The ASTM E606 procedure was employed for the uniaxial strain-controlled cyclic tests. The tests were carried out in a 100 kN Dynacell servo-hydraulic test system at 0.125 Hz frequency. The tests were started in compression to avoid buckling problems. The longitudinal strain was measured continuously throughout each test using a calibrated extensometer with a 10 mm gauge length attached to the specimen. The triangular waveform was used for the straining of the specimens as it provides a constant effective strain rate. The tests were run until the complete separation of the specimen into two parts. However, failure was defined based on a 50% tensile load drop, i.e. the ratio of the maximum tensile load at the cycle of failure goes below 50% of that at the first

Table 6
Experimental and predicted fatigue life using strain energy density approach.

ID	Strain range ($\Delta\varepsilon$)	Strain ratio (R_ε)	$N_{f.exp}$ [cycles]	$\Delta W_{p.HL}$ [MJ/m^3]	$\Delta W_{t.HL}$ [MJ/m^3]	$\Delta W_{p.sat}$ [MJ/m^3]	$N_{f.p}$ [cycles]	$\Delta W_{t.sat}$ [MJ/m^3]	$N_{f.t}$ [cycles]
Part 1	Experimental					Predicted (Numerical simulation)			
T1S6	0.008	−1	15041	1.33	2.23	1.30	15088	2.38	11123
T2S5	0.008	−1	9640	1.56	2.45	1.30	15088	2.38	11123
T3S3	0.009	−1	4489	2.19	3.16	2.16	7392	3.20	6755
T22S24	0.009	−1	7119	2.29	3.26	2.16	7392	3.20	6755
T4S2	0.012	−1	3022	4.67	5.72	4.64	2546	5.73	2598
T5S15	0.015	−1	1570	7.30	8.49	7.29	1355	8.52	1373
T23S7	0.015	−1	1058	8.27	9.42	7.29	1355	8.52	1373
T17S19	0.020	−1	646	12.38	13.76	13.06	601	14.41	593
Part 3									
T13S22	0.009	0.33	5768	2.79	3.68	2.14	7493	3.18	6814
T12S23	0.009	0	6438	2.50	3.41	2.15	7445	3.19	6779
T7S13	0.009	−0.33	4877	2.05	3.09	2.20	7210	3.23	6640

Table 7
Details of the applied nominal loads in FEM.

Loading	***PL*** [%*MBL*]	***ML*** [%*MBL*]	***CL*** [%*MBL*]
Case 1	**70**	16	8
Case 2	**70**	16	10
Case 3	**70**	20	8
Case 4	**70**	20	10

Table 8
Comparison of von Mises stress and maximum principal strain at the critical point on the pit wall at the maximum load of loading case 1 for different mesh densities.

	Coarse mesh	Average mesh	Fine mesh
No. of elements in the model	35419	38699	66713
Maximum von Mises stress [MPa]	862	882	890
Relative error in stress value wrt the fine mesh [%]	−3.1	−0.9	0
Location of maximum principal strain along the path A [mm]	0.00	0.56	0.53
Maximum principal strain	0.0059	0.0065	0.0069
Relative error in strain value wrt the fine mesh [%]	−14.9	−6.2	0

Table 9
Details of different loading cases and experimental and predicted fatigue life.

Nominal ***ML%MBL***	Nominal ***CL%MBL***	N_f*experimental* [cycle]	N_f*DNVGL* [cycle]	$N_{initiation}$*predicted* [cycle]	3rd order polynomial $ANi^3 + BNi^2 + CNi + D$				
					A(e−11)	B(e−9)	C(e−5)	D	R^2
16	8	501872[a]	520436	113418	2	8	20	36.9	0.998
16	10	318174[a]	266430	70936	7	200	40	36.9	1
20	8	–	520436	49250	20	−70	2	36.9	0.993
20	10	126614[b]	266430	48938	20	100	10	36.8	0.999

[a] Reported by Fredheim et al. in Ref. [40].
[b] Unpublished report.

cycle. The uniaxial experimental program includes 12 specimens successfully tested under five strain ranges ranging from 0.8% to 2% and four strain ratios of ($R_\varepsilon = \varepsilon_{min}/\varepsilon_{max}$) of −1, −0.3, 0, 0.3. Data from the tests with fractures outside of the gauge section of the specimens were considered invalid and excluded from data analyses. The test program was divided into 3 parts. 1) Single-step fully reversed ($R_\varepsilon = -1$), in which several specimens were tested at different strain ranges ($\Delta\varepsilon$) to investigate the strain range effect on the material cyclic response. 2) Multi-step fully reversed ($R_\varepsilon = -1$), where the sample was loaded at the strain range of 0.008 for a block of 1024 cycles followed by a block of 16 cycles at the strain range of 0.015, to study loading sequence effect. This strain sequence was repeated until the fracture of the specimen. 3) Single-step with different strain ratios, where the tests were conducted at the constant strain range of 0.009 but different strain ratios to study the effect of strain ratio on the mean stress relaxation. All experiments were conducted in room temperature and more than 200 data points per cycle were collected for data analyses.

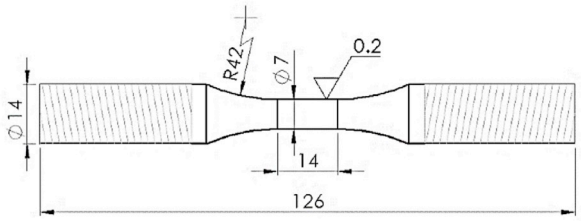

Fig. 1. The geometry of uniaxial fatigue test specimens, dimensions in mm.

2.2. Theoretical framework

2.2.1. Stress-strain relation

The monotonic stress-strain curve can be expressed by Ramberg-Osgood relation [28] as:

$$\varepsilon = \frac{\sigma}{E} + \left(\frac{\sigma}{K}\right)^{1/n} \tag{1}$$

where σ and ε are true stress and total strain values respectively, E is the elasticity modulus, K is the strain hardening coefficient, and n is the strain hardening exponent of the material.

Similar relation as in (1) can be written for the material's cyclic stress-strain curve based on the true stress-total strain curves at the half-life of cyclic test specimens (i.e. stable hysteresis loops) tested at different strain ranges with $R_\varepsilon = -1$, in other words, a locus of tips superposed by stable hysteresis loops at different strain ranges. Thus, the cyclic stress-strain amplitude relation is written as:

$$\varepsilon_a = \frac{\sigma_a}{E'} + \left(\frac{\sigma_a}{K'}\right)^{1/n'} \tag{2}$$

where σ_a and ε_a are true stress and total strain amplitudes respectively, E' is the cyclic elasticity modulus averaged for the all studied strain ranges, K' is the cyclic strain hardening coefficient, and n' is the cyclic strain hardening exponent of the material. $K, n,$ K' and n' are identified using the least square method and the corresponding values are listed in Table 3.

2.2.2. Strain-life relation

The test data Part 1, i.e. single-step and fully reversed tests, are analyzed on the basis of Basquin-Coffin-Manson (BCM) strain-life relationship as follows [29,30]:

$$\varepsilon_{ta} = \varepsilon_{ea} + \varepsilon_{pa} = \frac{\sigma_f'}{E}(2N_f)^b + \varepsilon_f'(2N_f)^c \tag{3}$$

where ε_{ta}, ε_{ea}, and ε_{pa} are, respectively, the total, elastic, and plastic strain amplitudes, σ'_f and ε_f' are the fatigue strength and ductility coefficients and b and c are the fatigue strength and ductility exponents of the material. These parameters are identified using the least square method and the corresponding values are listed in Table 4.

2.2.3. Cyclic plasticity modeling

The elastic-plastic response of the material is essential for accurate numerical simulations of the components experiencing cyclic plasticity whether in the global or local domain, e.g. mooring chains with pitted surfaces. Regardless of the methodology used to estimate the remaining fatigue life of pitted mooring chains, an advanced cyclic plasticity model is required to accurately identify stresses, strains, and SED at the chains pit site. Therefore, this part is dedicated to the cyclic plasticity modeling of the material under study.

The rate-independent non-linear plasticity model considered in the current work combines kinematic and isotropic hardening. Hence, the yield function (f), which governs the onset of the plastic deformation, is expressed as:

$$f = \phi(\boldsymbol{\sigma} - \boldsymbol{\chi}) - (\sigma_0 + R) \leq 0 \tag{4}$$

where $\boldsymbol{\sigma}$ and $\boldsymbol{\chi}$ are the stress and backstress tensors and assumed to be symmetric respectively, σ_0 refers to the yield stress at zero plastic strain, R denotes the isotropic work-hardening variable, and ϕ is the von Mises equivalent stress and is calculated, assuming that the material is isotropic and pressure insensitive, as follows:

$$\phi = \sqrt{\frac{3}{2}(\boldsymbol{\sigma}' - \boldsymbol{\chi}') : (\boldsymbol{\sigma}' - \boldsymbol{\chi}')} \tag{5}$$

where $\boldsymbol{\sigma}'$ and $\boldsymbol{\chi}'$ are the stress and backstress deviators respectively. Assuming small deformations, strains in an elastic-plastic model can be decomposed into elastic (reversible) and plastic (irreversible) parts using the Poisson's ratio and cyclic elastic modulus

presented in Tables 1 and 3 respectively. The isotropic work-hardening variable on the basis of Voce law reads:

$$\begin{aligned} R &= Q_\infty(1-\exp(-bp)) \\ \dot{R} &= h_R\dot{\lambda} \quad , \quad h_R = Q_\infty b\exp(-bp) \end{aligned} \tag{6}$$

where p is the equivalent plastic strain, h_R is the hardening modulus, Q_∞ and b are the saturated value of R and the rate of saturation achievement respectively, and $\dot{\lambda}$ denotes a non-negative scalar (the plastic multiplier). The associated flow rule assumes that plastic flow is in a direction normal to the yield surface at the load point and determines the plastic strain rate ($\dot{\boldsymbol{\varepsilon}}^{\mathbf{p}}$) as:

$$\dot{\boldsymbol{\varepsilon}}^{\mathbf{p}} = \dot{\lambda}\frac{\partial f}{\partial \boldsymbol{\sigma}} \tag{7}$$

where $\dot{\lambda} = \dot{p}$ and $\dot{p}$ is the von Mises equivalent plastic strain rate given by:

$$\dot{p} = \sqrt{\frac{2}{3}\dot{\boldsymbol{\varepsilon}}^{\mathbf{p}} : \dot{\boldsymbol{\varepsilon}}^{\mathbf{p}}} \tag{8}$$

Kinematic work-hardening that has been introduced to the yield function of the material through a backstress tensor is written based on Armstrong- Frederick parameters [31] as:

$$\begin{aligned} \dot{\boldsymbol{\chi}} &= c\dot{\boldsymbol{\varepsilon}}^{\mathbf{p}} - \gamma\boldsymbol{\chi}\dot{p} \\ \dot{\boldsymbol{\chi}} &= \mathbf{h}^{\boldsymbol{\chi}}\dot{\lambda} \quad , \quad \mathbf{h}^{\boldsymbol{\chi}} = c\frac{\partial f}{\partial \boldsymbol{\sigma}} - \gamma\boldsymbol{\chi} \end{aligned} \tag{9}$$

where $\mathbf{h}^{\boldsymbol{\chi}}$ is a second order tensor, c *and* γ are material parameters, and $\dot{\boldsymbol{\chi}}$ denotes the rate of backstress tensor. Using Hooke's law, the consistency condition ($\dot{\lambda}\cdot\dot{f} = 0$) determines the plastic multiplier:

$$\dot{\lambda} = \frac{\frac{\partial f}{\partial \boldsymbol{\sigma}} : \mathbf{C} : \dot{\boldsymbol{\varepsilon}}}{\frac{\partial f}{\partial \boldsymbol{\sigma}} : \mathbf{C} : \frac{\partial f}{\partial \boldsymbol{\sigma}} + \frac{\partial f}{\partial \boldsymbol{\sigma}} : \mathbf{h}^{\boldsymbol{\chi}} + h_R} \tag{10}$$

where $\mathbf{C}$ is the elastic stiffness matrix, and $\dot{\boldsymbol{\varepsilon}}$ is the total strain rate tensor. An implicit return-mapping algorithm has been used to provide a converged solution for the non-linear algebraic equations for expressing the non-linear hardening of the material.

To identify the kinematic and isotropic hardening parameters for the material under study, the procedure explained above has been scripted and run in MATLAB software. The parameters to be identified get initial values and used in the developed routine to simulate the stress-strain curves at cycles number 10, 100, and half-life to properly simulate both the transient and stabilized material cyclic response under strain range used in the test program part. The simulated curves are then compared with those from experiment at the corresponding cycles and the difference error is defined as the objective function to be minimized in an optimization algorithm. The MATLAB routine "fminsearchbnd" has been used for the optimization. Using this routine, the parameters can vary within defined ranges in the optimization process. The initial guesses, the lower, and the upper bands for the parameters used in the optimization algorithm as well as the sets of calibrated parameters providing optimized stress-strain curves at cycle 10, 100, and half-life at each strain range of the fatigue tests Part 1 are listed in Table 5.

2.2.4. Fatigue life prediction using strain energy density (SED)

The strain-life relation presented previously is generally applicable to the cases where there is no mean stress in the specimen or component. This type of loading, however, rarely exists in real applications. Unlike the strain-based or stress-based approaches, the SED approach is independent of the orientation of reference axes and, by accounting for stresses as well as strains, handles the cases with non-zero mean stress/strain in the same way it does to the cases with fully reversed stress/strain-controlled loadings. From low cycle fatigue (LCF) to high cycle fatigue (HCF) regimes, SED is able to explain complex phenomena tied with crack initiation and propagation and thus, is used here for fatigue life estimation of the specimens tested under uniaxial strain-controlled loading with various strain ranges and strain ratios and crack initiation from an existing pit on a pitted chain link.

The plastic SED at half-life (ΔW_p) can be expressed by a simple power law as a function of the number of reversals to failure ($2N_f$):

$$\Delta W_p = \alpha\left(2N_f\right)^{\beta} \tag{11}$$

where $\alpha = 2110\ MJ/m^3$ and $\beta = -0.717$ are the material parameters and for mooring chain steel grade R4 are identified by the best fit to the experimental data Part 1.

Alternatively, the total SED at half-life (ΔW_t), defined as the sum of plastic strain energy (ΔW_p) and elastic energy associated with the tensile stress ($\Delta W_{e+} = \sigma_{max}^2/2E$) to account for mean stress [32], can be contributed to the number of reversals to failure to estimate fatigue life. This approach is more suitable for HCF, where the plastic strain energy is too small to be accurately measured. Thus, the total SED is written as:

$$\Delta W_t = \alpha^{'}\left(2N_f\right)^{\beta^{'}} + \Delta W_0^t \tag{12}$$

where α', β' are material parameters and ΔW_0^t is the tensile elastic energy at the fatigue limit of the material. These parameters are

identified by the best fit to the experimental data Part 1 as $\alpha' = 1289\ MJ/m^3$, $\beta' = -0.637$ and $\Delta W_0^t = 0.17\ MJ/m^3$ corresponding to a stress amplitude of $\sigma_e = \sqrt{2 \cdot E \cdot \Delta W_0^t} = 255\ MPa$.

The variation of cumulative plastic strain energy (W_f) with the number of reversals to failure can be described by a simple power law similar to Eq. (11):

$$W_f = \alpha''(2N_f)^{\beta''} \tag{13}$$

where parameters $\alpha'' = 1166\ MJ/m^3$ and $\beta'' = 0.27$ are identified by best fit to the experimental data Part 1, 2, and 3.

3. Results

The summary of the fatigue test results is listed in Table 2 and various aspects of the material behavior under different loading conditions are discussed in this section.

3.1. Cyclic softening

Fig. 2a illustrates the stress amplitude variation as a function of normalized fatigue life at different strain ranges. A similar S-shape trend in the reduction of stress amplitude is seen for all strain ranges. This behavior is common among high strength metals and alloys due to obtaining lower energy dislocation arrangement. Quick reduction in the stress amplitude values (material softening) is observed in the first 10% of the specimens' lives, thereafter, the stress amplitudes tend to stabilize and remain almost constant up until approximately 90% of life. The final 10% of the specimens' lives are involved with high load carrying reduction mainly due to the growth of macroscopic cracks until final fracture. Similar behavior has been observed for high strength steel (DIN 34CrNiMo6) [33]. To quantify the cyclic softening of the material, a softening ratio (SR) is defined as:

$$SR = \frac{\sigma_{a,1} - \sigma_{a,\ half-life}}{\sigma_{a,1}} \tag{14}$$

where, $\sigma_{a,1}$ and $\sigma_{a,\ half-life}$ are the stress amplitude at the first and the half-life cycle of the specimens respectively. The softening ratio is about 22% and nearly independent from the applied strain range for the strain-controlled tests conducted in the test program Part 1, see Fig. 2b.

3.2. Masing-type behavior (strain range effect)

The stabilized hysteresis loops at the half-life of each specimen tested in Part 1 of the test program provide information on the Masing properties of the material. For a Masing-type material, the loading branches of hysteresis loops at different strain ranges coincide with the magnification of the stable cyclic stress-strain curve by a factor of two. To investigate this behavior of the material, the experimental stable cyclic stress-strain curves at different strain ranges are collected in a single graph with compressive tips coinciding at origin (0,0), as shown in Fig. 3. As seen from this, the material does not follow the Masing-type behavior and the stiffness of the material reduces as strain range increases. As a result, the estimation of the hysteresis loop area using the so-called "Masing curve" overestimates the SED at any arbitrary strain range and yields conservative predictions if an energy-based fatigue model is employed. The non-Masing behavior depends on the material as well as loading and is more pronounced at higher strain ranges [34].

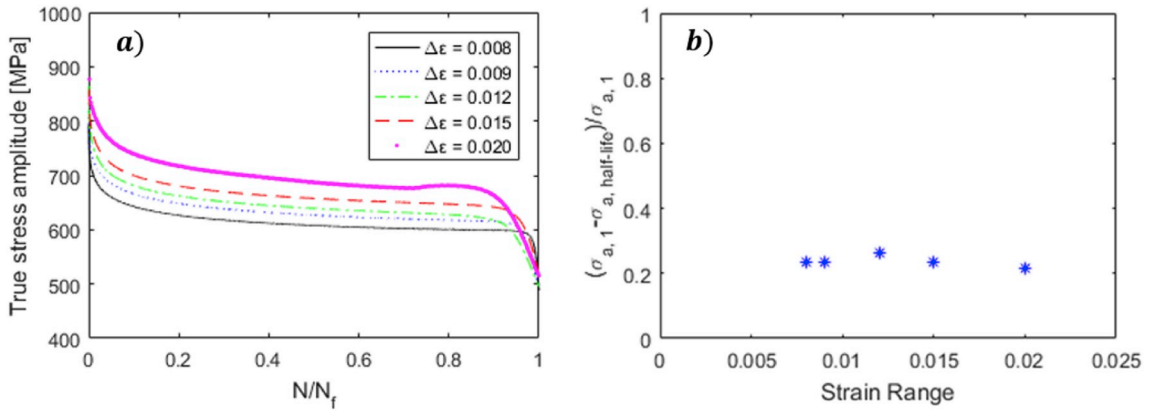

Fig. 2. a) Stress amplitude vs normalized fatigue life and b) softening ratio at various strain ranges.

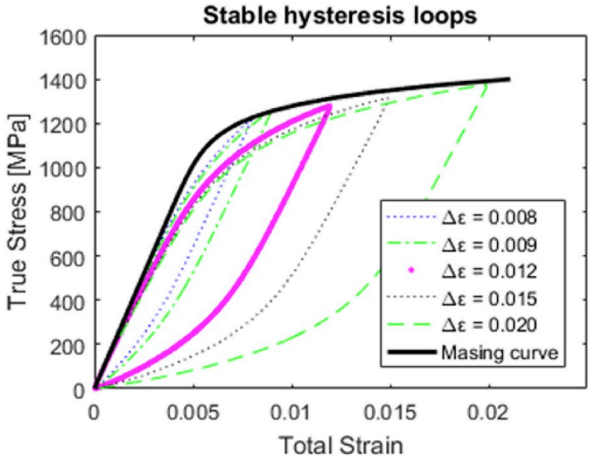

Fig. 3. Stable hysteresis loops at various strain ranges plotted in a relative coordinate system at which the maximum compressive stresses coincide.

3.3. Mean stress relaxation

Non-fully reversed strain-controlled loading condition results in non-zero mean stress (σ_m). As seen from Fig. 4a, the normalized mean stress versus the normalized life at different strain ratios follows nearly the same trend. Almost 90% of the initial mean stress is relaxed at the half-life of the specimens, where a huge part of the relaxation occurs approximately in the first 10% of the specimens' fatigue lives. This relaxation is mainly due to the cumulative plastic straining inside the material. Thus, a smoother relaxation is expected at lower strain ranges i.e. larger effect of mean stress on fatigue life in HCF regime. For the specimens made of the material under study and cyclically loaded at the strain range of 0.009 with strain ratios varying from −0.3 to 0.3, the mean stress relaxation trend follows an S-shape curve that is little influenced by the strain ratio, see Fig. 4a. However, the amount of relaxation is a linear function of the strain ratio, as shown in Fig. 4b.

3.4. Loading sequence effect

The load history effect is evaluated here by analyzing the data from the multi-step uniaxial strain-controlled fatigue test, in which the specimen experiences a strain block of 1024 cycles at the strain range of 0.8% followed by a strain block of 16 cycles at strain range of 1.5%. This sequence is repeated until the specimen fractures. Fig. 5a presents the variation of maximum, minimum and mean stresses values versus the number of cycles for both the multi-step and single-step tests. It is seen that the material experiences more overall softening, i.e. a 5% lower stabilized stress amplitude, in the multi-step test comparing to that in the single-step strain-controlled test at the strain range of 0.8%. The effect of overloading on the material softening decreases after the first few straining sequences and the stress amplitudes reaches to a stabilized value, see Fig. 5b.

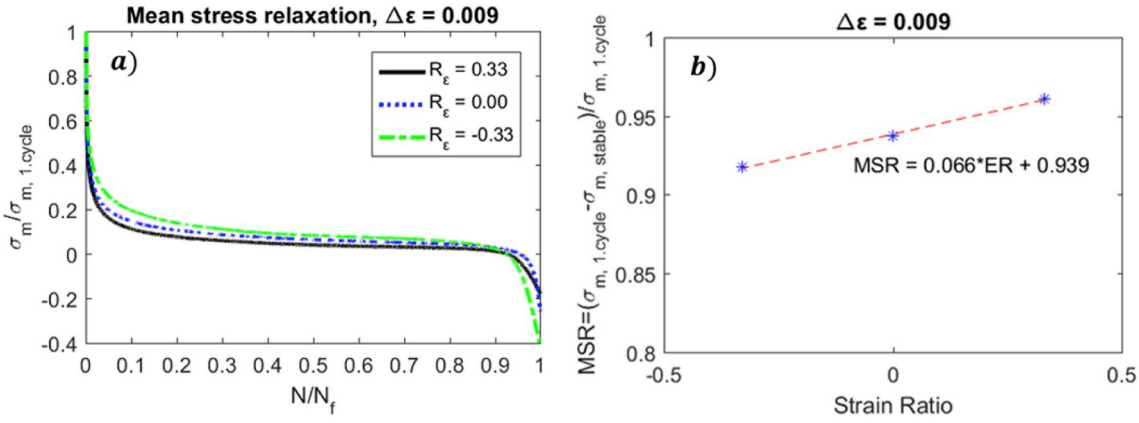

Fig. 4. a) normalized mean stress vs normalized life and b) mean stress ratio (MSR) as a function of strain ratio (ER).

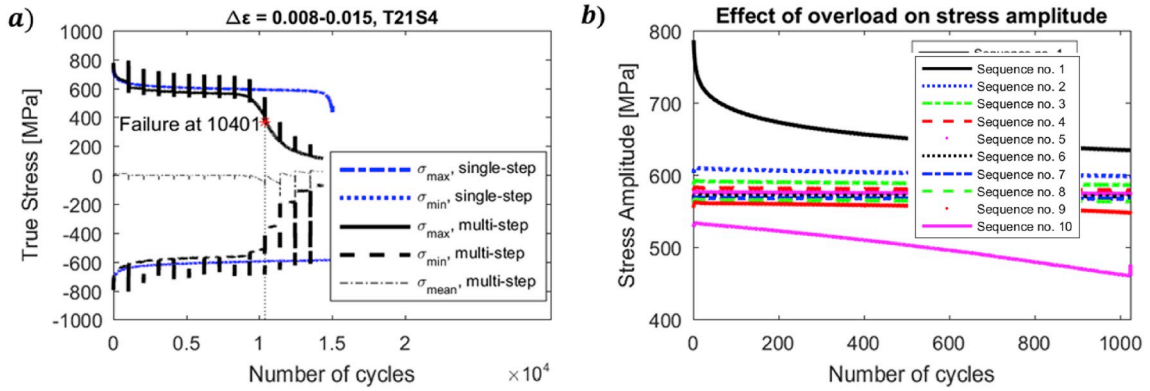

Fig. 5. a) multi-step test with lower strain range of 0.008 and higher strain range of 0.015 and b) the effect of overloading on stress amplitudes at each loading sequence (blocks of 1024 cycles).

3.5. Stress-strain relation

The monotonic and cyclic stress-strain curves in Ramberg-Osgood form, Eqs. (1) and (2), are illustrated in Fig. 6 and the identified parameters are listed in Table 3. It is seen that the cyclic stress-strain curve lays below the monotonic curve as a result of the material's cyclic softening. Hence, the use of a material model based on the monotonic response of the material in applications where components are expected to experience cyclic loading conditions, e.g. mooring chains, significantly underestimates the amount of plastic straining in the material and leads to inaccurate estimation of fatigue life. The cyclic elasticity modulus was calculated as the average value of the slope of the linear portion of the stable hysteresis loops upon strain reversal from the maximum load at different strain ranges. As this way of finding E differs from how the monotonic E is determined, a small difference is obtained.

3.6. Strain-life relation

Plastic, elastic, and total strain amplitudes as a function the number of reversals curves, Eq. (3), as well as the data points from the experimental data Part 1 are illustrated in Fig. 7. The transition life (N_T), at which elastic and plastic strain amplitudes are identical, is characterized as 2139 cycles. The strain-life curve of un-notched specimens can be used for the LCF as well as HCF analysis of notched components since fatigue damage is assessed directly in terms of local strains.

3.7. Cyclic plasticity modeling

Fig. 8 presents the comparison of numerical and experimental stress-strain curves at different strain ranges at cycles number 10, 100, and at half-life following the procedure presented in Section 2.2.3. For clarity, the hysteresis loops are partly presented. A decent agreement between the experimental and numerical stress-strain curves is observed. The stress amplitudes obtained from numerical simulations are similar to those from experimentations with a maximum difference of less than 5%. Further, a good approximation of energy dissipation during cyclic loading is achieved, which is valued for the prediction of the remaining fatigue life of notched components, e.g. pitted mooring chains, using an energy-based fatigue approach.

The comparison of the identified parameters for different strain ranges in Table 5 shows that the material cyclic hardening/

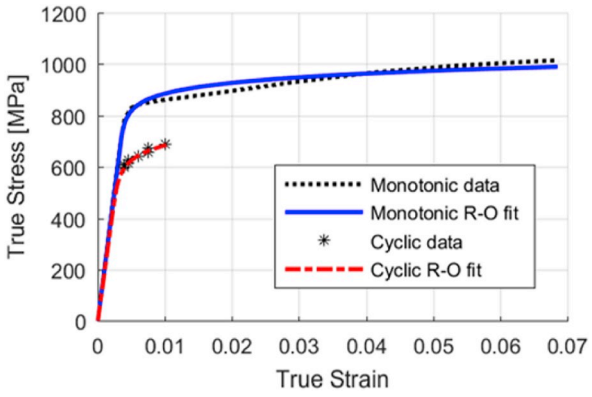

Fig. 6. Monotonic and cyclic stress strain curves for the chain material steel grade R4.

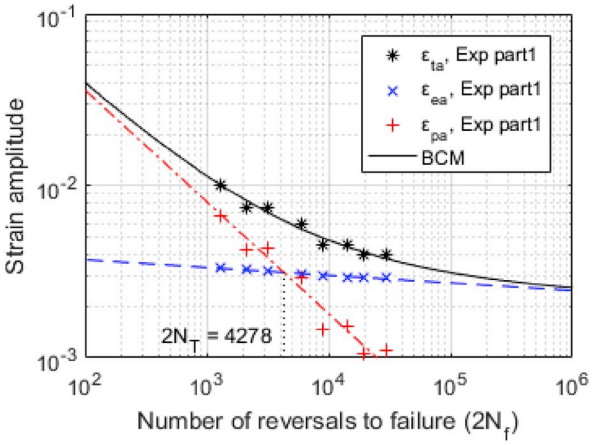

Fig. 7. Total strain (solid), plastic strain (dashdotted), and elastic strain (dashed) amplitudes vs number of reversals to failure for mooring chain steel grade R4.

softening cannot be described by a single set of hardening parameters due to the non-Masing type behavior of the material. Thus, to get the most accurate results from numerical simulation, one should use the set of variables for the strain range closest to that in the real application.

3.8. Fatigue life prediction

Eqs. (11) and (12) can be used for fatigue life estimation of specimens made of mooring chain steel grade R4 and the predictions are examined for several different strain ranges and strain ratios. Fig. 10a illustrates the SED-life curve for the material under study. SED could be obtained by averaging SED over the number of cycles to failure or closely approximated by the SED at the half-life cycle of each specimen.

The fatigue lives of the specimens tested in the fatigue test program Part 1 and Part 3 are estimated using the plastic and total SED at half-life (HL) obtained from numerical simulations in Eqs. (11) and (12) and are denoted by $N_{f,p}$ and $N_{f,t}$ respectively. The estimated lives are compared with the experimental lives and listed in Table 6. Fig. 9 illustrates how successfully the SED approach can correlate the predicted and experimental lives of the specimens over the entire range of applied strain ranges and ratios. In practice, fatigue life can be estimated using both plastic and total SED with decent accuracy, and in this investigation, the predicted lives are within a factor of 1.7 of the experimental lives.

As seen in Fig. 10b, a higher amount of plastic strain energy is accumulated prior to failure at lower strain ranges and vice versa. In other words, fatigue toughness of the material increases as the applied dynamic load decreases. Knowing the stable plastic SED, i.e. the energy dissipation at half-life (ΔW_p), for a specimen made of the material under study, one can get a rough estimation of the number of reversals to failure using Eq. (13) by substituting W_f with $\Delta W_p{}^* N_f$. It is worth noting that the results from test Parts 2 and 3 are also added to the graph presented in Fig. 10b, showing that the SED approach can properly account for variable amplitude loading as well as mean load effect. For instance, the number of loading blocks to failure (N_b) for the specimen in fatigue test Part 2 can be estimated using the stable plastic SED and cumulative plastic SED at the strain range of 0.008 and 0.015 and Palmgren-Miner rule:

$$N_b{}^*\left[1024{}^*\left(\frac{\Delta W_{p\ at\ \Delta\varepsilon=0.008}}{W_{p\ at\ \Delta\varepsilon=0.008}}\right)+16{}^*\left(\frac{\Delta W_{p\ at\ \Delta\varepsilon=0.015}}{W_{p\ at\ \Delta\varepsilon=0.015}}\right)\right]=1$$

$$N_b = 10.02\ blocks$$

and knowing that each block had 1040 cycles the number of cycles to failure can be estimated as $N_f = N_b{}^*1040 = 10421$ cycles that is comparable with the experimental life which is 10401 cycles.

4. Case study; finite element simulation of pitted mooring chains

Fatigue cracks initiation is generally due to cyclic plastic straining. Hysteresis loop area versus life curve has been shown to be effective in the fatigue life estimation of un-notched specimens at various loading conditions. The remaining life of corroded mooring chains that experience local plastic straining around the pitting holes at the surface can be estimated in the same manner. Thus, a cyclic elastic-plastic material model is essential for accurate simulation of plastic straining at the mooring chain pit site. Such a model is herein proposed based on the obtained material hardening parameters following the procedure presented in 2.2.3. The parameters at the strain range of 0.009 are chosen to be representative for all strain ranges. The implementation of a material model based on these parameters provides a decent prediction of the material cyclic behavior at loads levels near the material yield point and acceptable predictions at higher loads. The model combining kinematic with isotropic hardening based on Armstrong-Frederick and Voce

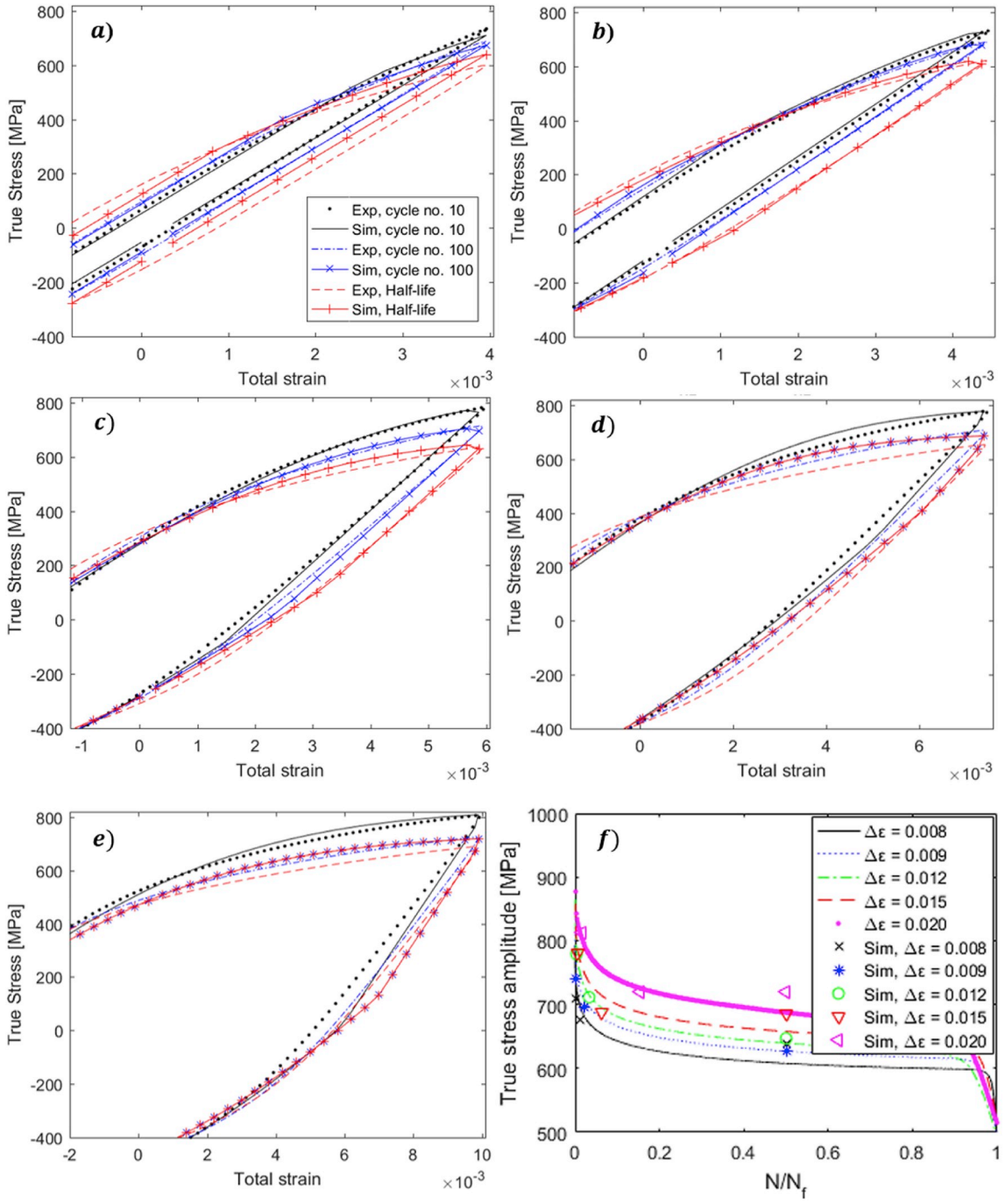

Fig. 8. Visualization of the material cyclic response at cycle no. 10, 100, and half-life (saturated) at the strain ranges of a) 0.008, b) 0.009, c) 0.012, d) 0.015, e) 0.020, f) stress amplitudes; numerical simulation using the optimized hardening parameters vs experimental.

parameters is implemented in Abaqus software and utilized in plastic deformation analysis at the pit sites on chain links.

A model consisting of one complete chain link with the diameter (D) of 114*mm* and two half links are constructed. To reduce the computational efforts, only 1/8 portion of the model with three symmetry planes (XY, YZ, XZ) are used in the analysis, see Fig. 11. Hard contact with the penalty method with a stiffness scale factor of 0.01 is applied to the chains contact regions to lower over-constraint issues and reduce the number of iterations required in the analysis [35]. A friction coefficient of 0.3 is used for the tangential behavior of the interaction [36].

First order hexahedral elements with reduced integration schemes (C3D8R) are used, and mesh convergence has been carried out with a finer mesh at the pit site in order to capture plastic strain localization optimally. Fig. 13 illustrates the maximum principal strain

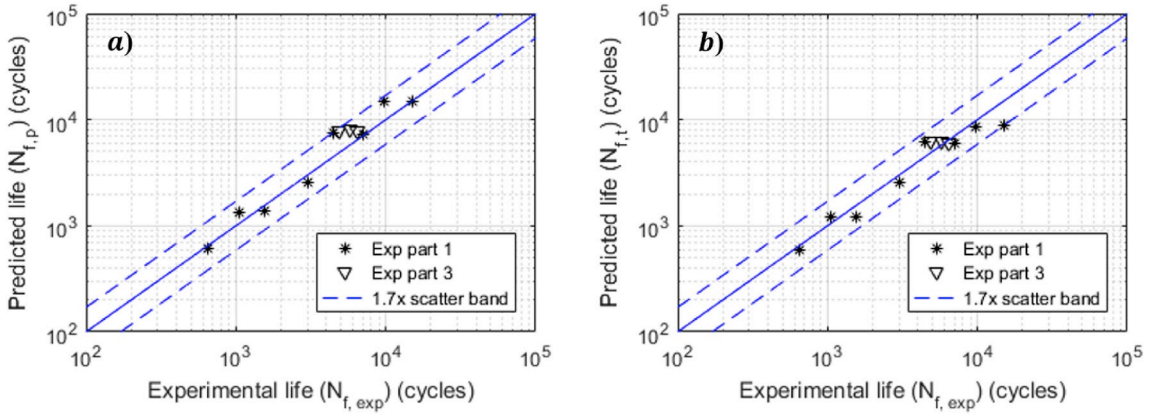

Fig. 9. Experimental vs predicted fatigue life based on SED approach using a) ΔW_p and b) ΔW_t obtained from numerical simulations.

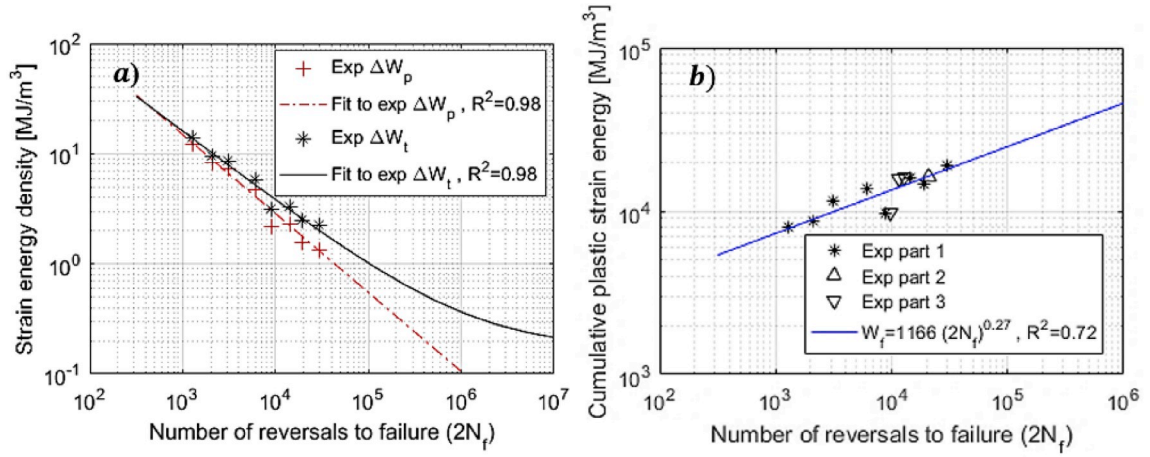

Fig. 10. a) plastic strain energy density (dashdotted) and total strain energy density (solid) and b) cumulative plastic strain energy (W_f) vs number of reversals to failure ($2N_f$).

contours at the pit site at the chain crown for three different mesh sizes, and maximum principal strains along path A are compared and presented in Fig. 13d. It is seen that the strain is more localized at the pit wall rather than the pit bottom for the considered hemispherical pit at the chain crown. Table 8 compares von Mises stress and maximum principal strain at the critical point located at the pit wall. Considering the mesh study results presented in Table 8 and Fig. 13, the model with average mesh size is able to efficiently determine stress and strain values as well as the location of the critical point at the pit site (i.e. on the pit wall) with acceptable accuracy and thus, used in the rest of the simulations.

To assess the effectiveness of the application of SED approach for the case of pitted mooring chains, a simplified case (mooring chains with smooth surfaces pitting holes) is considered herein and the effect of surface roughness inside corrosion pits is thus neglected as to date there is no data to characterize the average roughness at a typical mooring chain link corrosion pit surfaces. Three hemispherical pits with 4 mm depth ($a = 4mm$) and aspect ratio (AR) of 0.5 are introduced to the model after proof load removal. This is done, using the model change interaction in Abaqus/Standard, by deactivating elements in the pits to simulate material removal. The choices of the locations, depth, and aspect ratio of the pits are made based on the information obtained from the investigation of the recovered mooring chain links after several years of service life [23,37–39]. The modeled pits are located at the crown, the connection of the straight with the bent part (known as the K_t point), and the straight part of the middle chain link. This is to investigate crack initiation from corrosion pits at the critical fatigue failure locations on a typical studless mooring chain. In this relation, two paths are defined at the pit site; one at the pit wall and the other at the pit front of all the three pits, see Fig. 11c.

The loading and boundary conditions are shown in Fig. 11. The load is applied at a reference point (RP), which has restricted degrees of freedom in all directions except along the loading axis i.e. X-axis. The degrees of freedom of the half-chain cross-sections (loaded faces) at the straight parts are kinematically coupled to those of the RP except along the Y-axis. The nominal load (the force applied on the cross-section area at the chain link straight parts) history is detailed in Fig. 12 and Table 7 consisting of proof loading (PL), i.e. loading up to 70% of minimum breaking load ($MBL = 12420KN$) and unloading as defined in the standards [5], followed by a service load, which includes a mean load (ML) and a cyclic load (CL) caused by wind, wave, and seawater current. In this study,

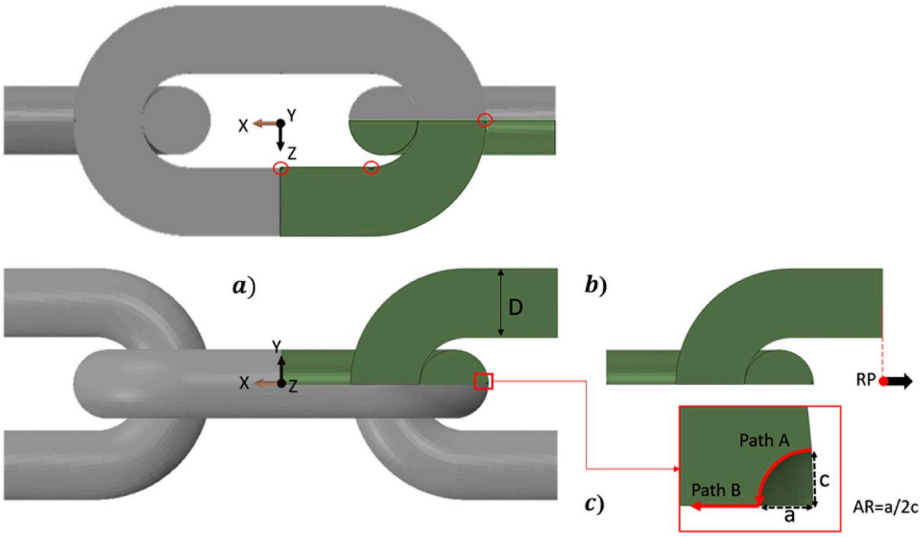

Fig. 11. a) finite element model of chain links with pits at three locations (red circles) on the considered 1/8 of the entire volume (shaded) b) loading point interacted with the loaded face, and c) pits geometry and the defined paths.

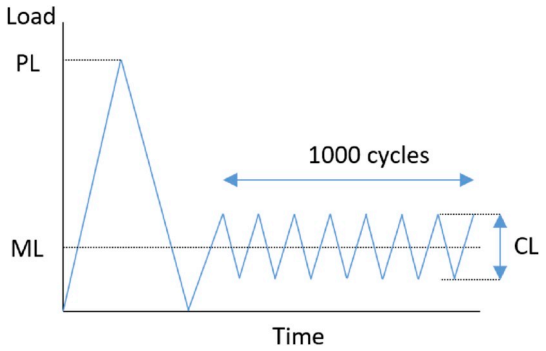

Fig. 12. Loading history applied in FEM for all considered loading cases.

different service load levels based on what mooring chains experience during their service lives are used to investigate the effects of mean tension and the load amplitude on plastic straining at the pit site. Note that the cyclic load levels correspond to extreme storm situations and also correspond to the load levels employed in large-scale testing in order to have manageable test durations.

Investigation of von Mises equivalent plastic strain (herein denoted by PEEQ) at the pit sites is beneficial in the identification of the location of crack initiation from the considered pits. Fig. 14 illustrates PEEQ variation at the wall (path A) and the front (path B) of the pits located at three different locations on the modeled chain link after being loaded for 1000 cycles of a service load (ML = 16%, CL = 8% of MBL). Similar trends have been observed at the other service loading cases studied here. It is seen that the highest amount of plastic strain accumulation, almost 3 and 6 times higher than that for the pit at the K_t point and the pit at the straight part of the link respectively, is around the pit located at the chain crown highlighting the fact that this site is the most critical location for fatigue cracks on a pitted mooring chain link. Many fatigue failures have been observed at the outer radius of corroded chain crowns in large-scale fatigue tests and reported elsewhere [23,38,40]. In view of this, assuming the single dominant flaw approach, we will concentrate on the pit located at the chain crown for the rest of this paper.

A closer look at the pit located at the chain crown provides an indication of where the crack will initiate from a hemispherical pit. The comparison of PEEQ at the pit wall before and after 1000 cycles of service load shows that the plastic strain accumulation rate is maximum at a location slightly below the pit mouth, where PEEQ has also its maximum value, as shown in Fig. 15c. This trend has been observed for other pit aspect ratios as well [21]. Accordingly, it is expected that cracks initiate from this location and grow until they enclose the hemispherical pit and further grow until the final fracture. Looking at the variation of PEEQ at the pit front in Fig. 15b, it is observed that a larger amount of material at the pit front experiences dynamic plastic straining as the material cycles. This results in an enlarged cyclic plastic zone and thus, higher mean stress relaxation within that zone influencing the crack growth rate at the chain crown.

FE simulations have been carried out to investigate energy dissipation at the pit site located at the chain crown under different loading cases. The accumulated energy dissipated per unit volume in the critical element by plastic deformation (W_p) for the first 1000

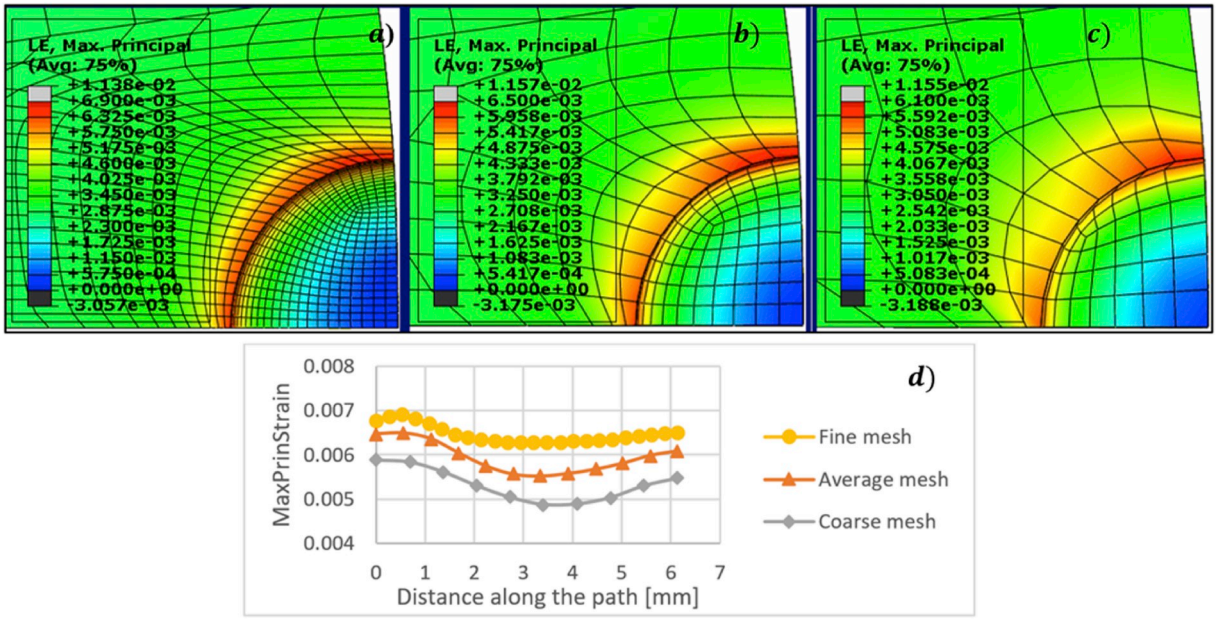

Fig. 13. Local mesh at the pit site at the crown with stress contours of a) fine,b) average, c) coarse mesh, and d) comparison of maximum principal strain along path A at the maximum load of loading case 1.

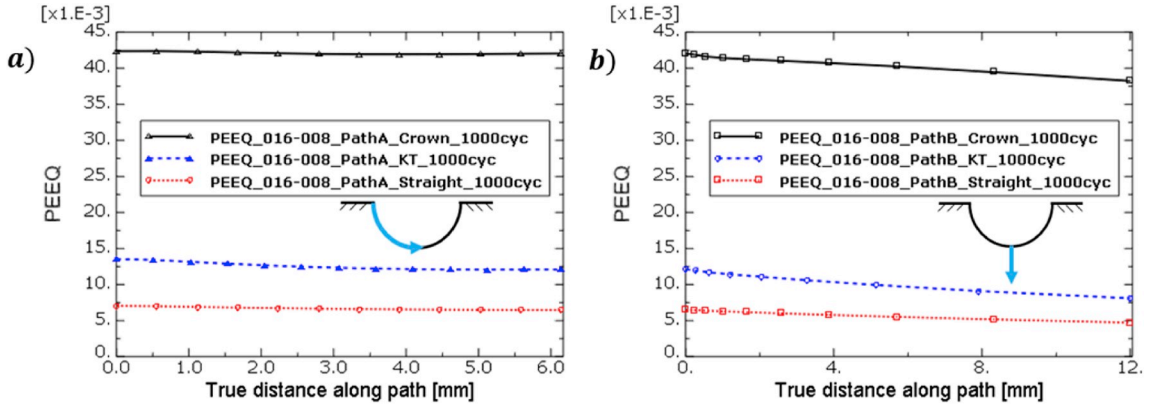

Fig. 14. Comparison of the equivalent plastic strain (PEEQ) along a) path A and b) path B for the three pits located at different locations on a chain link after being loaded for 1000 cycles.

cycle simulations at each loading condition is extracted and later extrapolated to one million cycles using polynomial fitting curves. These curves are then plotted together with the fitted curve to the W_p from the uniaxial small-scale tests and illustrated in Fig. 16. Since the plastic zone at the pit site is fairly constrained by the elastic material around it, the loading condition at the pit site can be assumed to be strain-controlled. Therefore, it can be assumed that the same amount of damage is accumulated at the gauge section the fatigue specimens and at the critical location at the pit site. Thus, both will have the same life to failure (corresponding to an initiated crack size of 3.5 *mm* i.e. the half diameter of the small-scale specimens) if W_p at the critical point in the pit site is equal that for the fatigue specimens. Although, this is a finite crack, it is small compared to the dimensions of the chain link. Accordingly, the intersections of the curves in Fig. 16 give the estimated number of cycles to crack initiation for the pitted chain link studied here.

To find out what order polynomial provides the most precise extrapolation, the simulation of the chain links at loading case 1 was continued to 10000 cycles and the resulted W_p is plotted, see Fig. 17, against that obtained from the simulation of the first 1000 cycles, which is extrapolated to 10000 cycles. It is seen that using a third-order polynomial fitting curve one can find out the trend of the cumulative dissipated energy for a higher number of cycles well. Hence, the simulations at the other loading cases were only continued to 1000 cycles to maintain the computational efforts cost-effective. The identified parameters for the fitting curves for each loading case are listed in Table 9.

The predicted lives using this energy-based approach as well as experimental fatigue lives of the corroded chain links ($D = 114mm$,

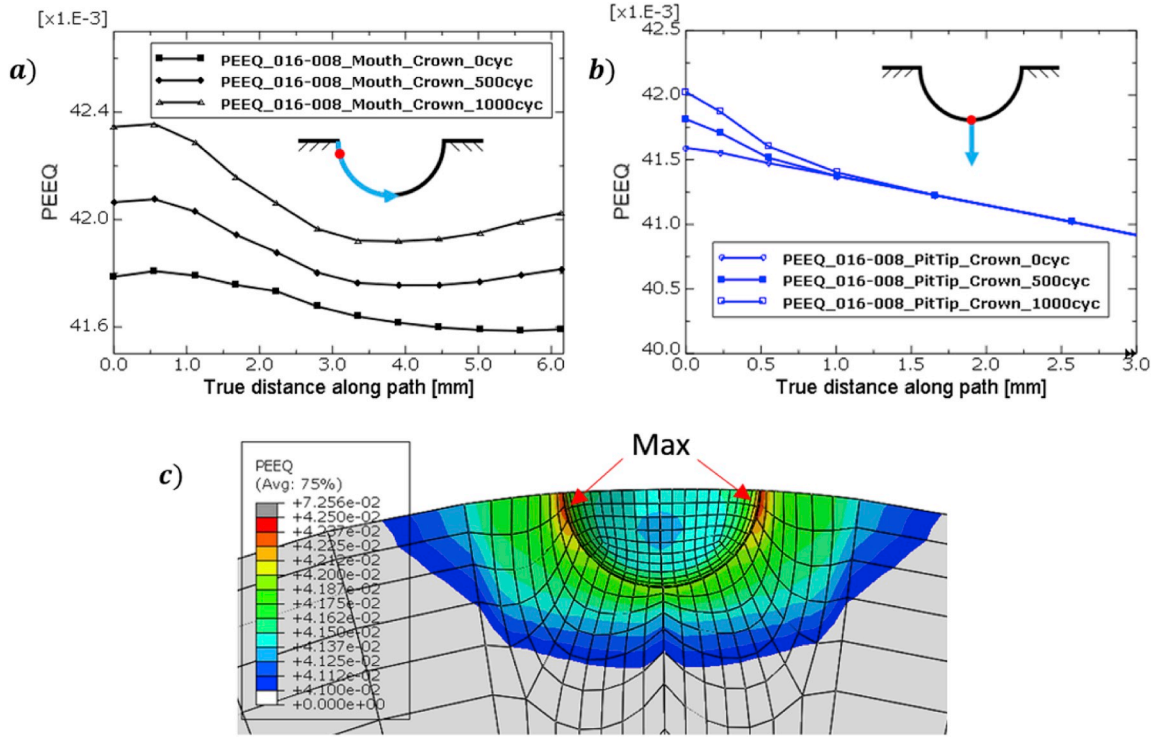

Fig. 15. Plastic strain accumulation along a) path A, b) path B for the pit located at the crown of a chain link before, during, and after 1000 cycles of service load (ML = 16%, CL = 8% of MBL), and c) PEEQ contour plot of the pit after 1000 cycles.

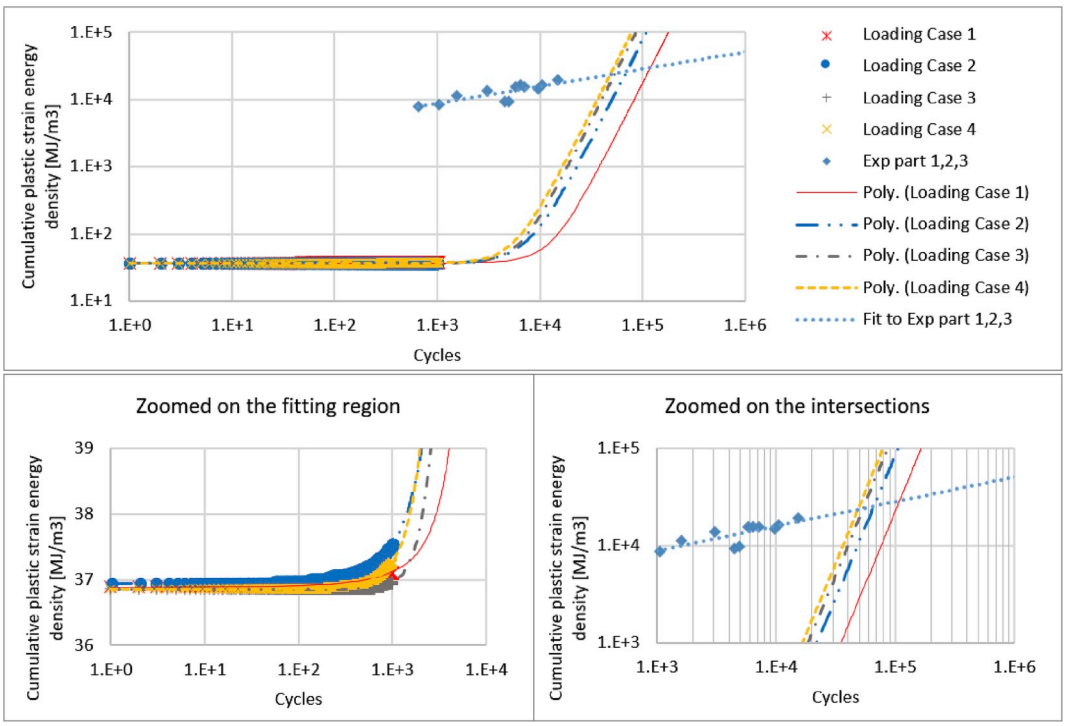

Fig. 16. Polynomial fit to the maximum plastic energy dissipation at slightly below the pit mouth vs number of cycles at different loading cases.

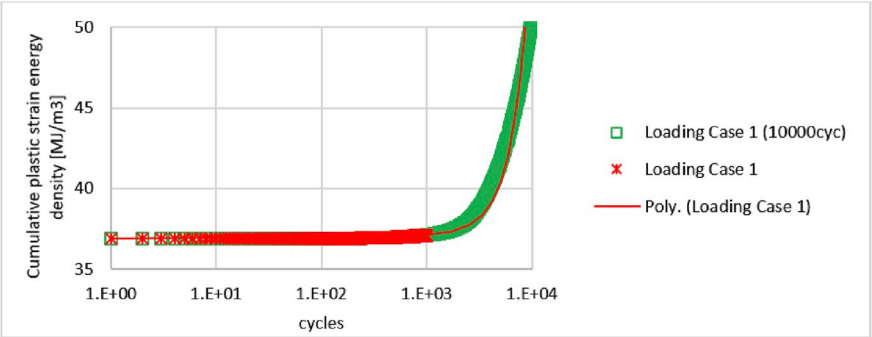

Fig. 17. The comparison of results from the simulation of the first 1000 vs 10000 cycles for loading case 1.

grade R4) tested in simulated seawater in the lab (3.5% sodium chloride) and predictions using S–N curves presented in DNVGL–OS–E301 [22] are listed in Table 9. In the large-scale tests, the failure was defined as a through thickness crack. The presented model provides predictions of crack initiation life from a pit at the surface of corroded chain links at different loading cases studied here. The estimated crack initiation life is about 20–40% of the experimental total life depending on the applied load. It is worth noting that unlike the DNVGL S–N curve, the model can account for the effect of the mean load as well as the load amplitude on the fatigue life of corroded mooring chains. It is seen from the predicted lives in Table 9 that the mean load has a larger effect than the load amplitude on the fatigue crack initiation life of pitted chains subjected to the loading cases studied here. For example, comparing loading case 1 with 3, a 25% increase in the mean load at the load amplitude of 8% MBL resulted in a 57% decrease in the predicted crack initiation life while comparing loading case 1 with 2, a 25% increase in the load amplitude made the initiation life only 37% shorter. The reduction in the initiation life at a higher load amplitude (10% MBL) for the same amount of increase in the mean load is less pronounced, almost 30%, but still highly noticeable.

A recent numerical study on the fatigue crack growth in mooring chains considering the residual stresses due to proof loading has been carried out in Ref. [41]. One can employ their methodology to estimate the number of cycles needed for a crack with a certain initial size to grow and cause failure in a chain link. The cycles are later added to the number of cycles predicted by the present approach for crack initiation from a pit to provide an estimation for the total life of a corroded chain link.

5. Summary and conclusion

Cyclic plasticity and fatigue performance of the mooring chain high strength steel grade R4 has been investigated using the data obtained from uniaxial strain-controlled fatigue tests on LCF specimens. The tests were divided into three parts; 1) single-step tests with the strain ratio of -1 and different constant strain ranges, 2) multi-step test with the strain ratio of -1 and varying strain amplitudes, and 3) tests with a constant strain range but different strain ratios. A non-linear combined kinematic and isotropic hardening model based on Armstrong-Frederick and Voce parameters has been used and calibrated to the experimental stress-strain curves. The calibrated material model has been employed in finite element simulations of pitted mooring chains at different service load levels to investigate plastic straining at the pit sites and estimate the number of cycles for a pit to crack transition. Strain-energy based fatigue approach has been used to estimate the fatigue life of the tested specimens as well as pitted mooring chains. The methodology developed here can be used to assess the serviceability of notched components, in this case, mooring chains. The following are some important observations from this study.

- Analysis of the data from the test program Part 1 has revealed that the material experiences rapid cyclic softening for all strain ranges studied. The softening trend has not been influenced by the applied strain range and the softening ratio was almost constant and equal to 25% in all the tests. This lower strength of the material under cyclic load is especially important to the analysis of fatigue cracks initiation and propagation in the applications in which the component experiences near yield cyclic loadings e.g. pitted areas of mooring chains.
- The material's fatigue and hardening parameters have been identified using the test data Part 1. The cyclic elastic-plastic response of the material using the identified parameters has been numerically evaluated and showed to be in a good agreement with the test data. The material exhibits non-Masing behavior. Thus, the material cyclic stress-strain curves at different strain ranges cannot be numerically simulated using a singular set of hardening parameters. Hence, different sets of hardening parameters have been identified for different cyclic strain ranges.
- Analysis of the data from test Part 3 revealed that the trend of the mean-stress softening was similar for the specimens tested in the same strain range but different strain ratios. However, the amount of softening is directly proportional to the strain ratio.
- The strain energy density (SED) approach has been employed to estimate the fatigue life of the specimens. A decent agreement was observed between the experimental and the predicted fatigue life estimated using plastic and total SED obtained from numerical simulations.

- The calibrated non-linear material model has been used in the FE simulation of pitted mooring chains subjected to different cyclic loading cases. The pit at the chain crown has been identified as the most critical pit among the considered pits in the FE model. This statement is supported by the observed failure locations on fatigue tested corroded chain links. Closely looking at the pits, the maximum equivalent plastic strain has been observed at a location slightly below the mouth of this pit.
- Fatigue crack initiation from a pit on corroded chain links has been predicted employing the calibrated material model in FEM and SED approach. The predicted life is about 20–40% of the total life of corroded chain links tested in the lab. The effect of the mean load on the crack initiation life of corroded chains has been successfully captured and recognized to be larger than the effect of the load amplitude for the loading cases considered in this work.

Declaration of competing interest

None.

Acknowledgement

The authors would like to acknowledge Equinor for providing the test material and financially supporting the experiments through the project KPN Lifemoor (RCN contract No: 280705), and the laboratory staffs at the structural engineering department of NTNU for their diligent work in performing the tests.

References

[1] Fontaine E, et al. Industry survey of past failures, pre-emptive replacements and reported degradations for mooring systems of floating production units. In: Offshore technology conference. Offshore Technology Conference; 2014.
[2] Ma K-t, et al. A historical review on integrity issues of permanent mooring systems. In: Offshore technology conference. Offshore Technology Conference; 2013.
[3] Apos R Souza, Majhi S. Application of lessons learned from field experience to design, installation and maintenance of FPS moorings. In: Offshore technology conference. Offshore Technology Conference; 2013.
[4] ISO19901-7:2013, Stationkeeping systems for floating offshore structures and mobile offshore units, in part 7 of Petroleum and natural gas industries specific requirements for offshore structures.
[5] DNVGL. Offshore standard DNV-OS-e302 offshore mooring chain. DNV GL AS; 2015.
[6] Perez IM, Bastid P, Venugopal V. Prediction of residual stresses in mooring chains and its impact on fatigue life. In: ASME 2017 36th international conference on ocean, offshore and arctic engineering. American Society of Mechanical Engineers; 2017.
[7] Bastid P, Smith SD. Numerical analysis of contact stresses between mooring chain links and potential consequences for fatigue damage. In: ASME 2013 32nd international conference on ocean, offshore and arctic engineering. American Society of Mechanical Engineers; 2013.
[8] Pacheco PMCL, et al. Finite element residual stress analysis applied to offshore studless chain links. ASME 2004 23rd international conference on offshore mechanics and arctic engineering. American Society of Mechanical Engineers; 2004.
[9] Pacheco PMCL, et al. Analysis of the influence of mechanical properties on the residual stress in offshore chain links using the finite element method. ASME 2003 22nd international conference on offshore mechanics and arctic engineering. American Society of Mechanical Engineers; 2003.
[10] Pérez-Mora R, et al. Very high cycle fatigue of a high strength steel under sea water corrosion: a strong corrosion and mechanical damage coupling. Int J Fatigue 2015;74:156–65.
[11] Stiff JJ, Smith DW, Casey NF. Fatigue of mooring chain in air and water - results and analysis. In: Offshore technology conference. Offshore Technology Conference; 1996.
[12] Crapps J, et al. Strength assessment of degraded mooring chains. In: Offshore technology conference. Offshore Technology Conference; 2017.
[13] Rosen J, et al. Chain FEARS JIP: finite element analysis of residual strength of degraded chains. In: Offshore technology conference. Offshore Technology Conference; 2015.
[14] Gao Z, Moan T, Heggelund SE. Time variant reliability of mooring system considering corrosion deterioration. ASME 2005;2005(41960):203–10.
[15] Huang Y, Tu S-T, Xuan F-Z. Pit to crack transition behavior in proportional and non-proportional multiaxial corrosion fatigue of 304 stainless steel. Eng Fract Mech 2017;184:259–72.
[16] Huang Y, et al. Numerical investigation of stress concentration factor at irregular corrosion pit under tension-torsion loading. In: ASME 2014 pressure vessels and piping conference. American Society of Mechanical Engineers; 2014.
[17] Huang Y, et al. Quantitative correlation between geometric parameters and stress concentration of corrosion pits. Eng Fail Anal 2014;44:168–78.
[18] Cerit M, Genel K, Eksi S. Numerical investigation on stress concentration of corrosion pit. Eng Fail Anal 2009;16(7):2467–72.
[19] Turnbull A, Horner DA, Connolly BJ. Challenges in modelling the evolution of stress corrosion cracks from pits. Eng Fract Mech 2009;76(5):633–40.
[20] Horner DA, et al. Novel images of the evolution of stress corrosion cracks from corrosion pits. Corros Sci 2011;53(11):3466–85.
[21] Xu S-h, Wang Y-d. Estimating the effects of corrosion pits on the fatigue life of steel plate based on the 3D profile. Int J Fatigue 2015;72:27–41.
[22] DNVGL. Offshore standard DNVGL-OS-E301 Position mooring. DNV GL AS; 2015.
[23] Gabrielsen Ø, Larsen K, Reinholdtsen S-A. Fatigue testing of used mooring chain. ASME 2017;2017(57632). V001T01A072.
[24] Totten, G., M. Howes, and T. Inoue, Handbook of residual stress and deformation of steel. ASM International.
[25] Zhang Y, Zettlemoyer N, Tubby P. Fatigue crack growth rates of mooring chain steels. In: Proc. ASME 2012 31st intl conf. Ocean. Offshore and Arctic Engineering; 2012. OMAE2012-84223.
[26] ASTM. E606/E606M-12, Standard test method for strain-controlled fatigue testing. ASTM international. West Conshohocken (PA USA): Book of Standards; 2012. p. 3.
[27] Rampi L, et al. Chain out of plane bending (OPB) fatigue joint industry project (JIP) FEA results and multiaxiality study results. ASME 2016;2016(49927). V001T01A002.
[28] Ramberg W, Osgood WR. Description of stress-strain curves by three parameters. 1943.
[29] Manson SS. Behavior of materials under conditions of thermal stress. National advisory committee for Aeronautics; 1954.
[30] Coffin Jr LF. A study of the effects of cyclic thermal stresses on a ductile metal, vol. 76. New York: Transactions of the American Society of Mechanical Engineers; 1954. p. 931–50.
[31] Armstrong PJ. A mathematical representation of the multiaxial Bauschinger effect. CEBG Report RD/B/N 1966;731.
[32] Golos K, Ellyin F. Generalization of cumulative damage criterion to multilevel cyclic loading. Theor Appl Fract Mech 1987;7(3):169–76.
[33] Branco RC, J D M, Antunes FV, Perdigão S. Monotonic and cyclic behavior of DIN 34CrNiMo6 tempered alloy steel. Metals 2016;6(5):98.
[34] Jiang Y, Zhang J. Benchmark experiments and characteristic cyclic plasticity deformation. Int J Plast 2008;24(9):1481–515.
[35] ABAQUS V. 6.14 documentation. Dassault Systemes Simulia Corporation; 2014.

[36] Rampi L, et al. Chain out of plane bending (OPB) fatigue joint industry project (JIP) static test program and OPB interlink stiffness. In: ASME 2016 35th international conference on ocean, offshore and arctic engineering. American Society of Mechanical Engineers; 2016.
[37] Fontaine E, et al. Investigation of severe corrosion of mooring chain in west african waters. In: The twenty-second international offshore and polar engineering conference. International Society of Offshore and Polar Engineers; 2012.
[38] Fernández J, Storesund W, Navas J. Fatigue performance of grade R4 and R5 mooring chains in seawater. In: ASME 2014 33rd international conference on ocean, offshore and arctic engineering. American Society of Mechanical Engineers; 2014.
[39] Fontaine E, et al. Scorch jip - feedback on MIC and pitting corrosion from field recovered mooring chain links. In: Proceedings of the annual offshore technology conference; 2014.
[40] Fredheim S, et al. Corrosion fatigue testing of used, studless, offshore mooring chain. In: OMAE2013-10609. Nantes: 32nd international conference on ocean, offshore and arctic engineering; 2013.
[41] Aursand, M. and B. Skallerud. Numerical simulation of fatigue crack growth in offshore mooring chains. in 10. National Conference on computational mechanics, MekIT'19. 2019. Norway: CIMNE.